Effects of Three-Dimensional Geometry and Collisions on Zonal Flows and Ion Temperature Gradient Modes in Helical Systems

M. Nunami[1], T.-H. Watanabe[1,2], and H. Sugama[1,2]

[1]National Institute for Fusion Science / [2]The Graduate University for Advanced Studies, Toki, Gifu, 509-5929, Japan

e-mail contact of main author: nunami.masanori@nifs.ac.jp

Abstract. Effects of three-dimensional geometry of the field configuration and collisions on the zonal flows and the ion temperature gradient (ITG) modes in the Large Helical Device (LHD) are investigated by using a newly developed gyrokinetic simulation code, GKV-X. The GKV-X incorporates full geometrical information such as the Jacobian and the metric tensor of the flux surface obtained from MHD equilibrium. The effects of the full geometry on the growth rate and real frequency of the ITG instability are clearly found in the large poloidal wavenumber region where the finite gyroradius effect is also important. The weak collision under the LHD experimental conditions reduces the residual zonal flow level, even if the geodesic acoustic mode oscillation as well as the growth rate and the real frequency of the ITG modes are not much affected. Furthermore, the simulation results for the linear ITG modes are compared with a high ion temperature discharge in the LHD experiments. It is found that the unstable ITG modes have the growth rates which peak at radial positions with the largest deviation of the temperature gradient from the critical values, where the peak positions of the growth rate are close to the regions where the density fluctuation peaks are measured in the experiment.

1. Introduction

Anomalous transport of the plasmas, which can be driven by the drift wave plasma turbulence [1] such as the ion temperature gradient (ITG) turbulence, has been a central issue in magnetic fusion research for the last few decades. The zonal flows are known to play a significant role in regulating the turbulent transport in toroidal plasmas [2–4]. It is shown by nonlinear gyrokinetic simulation with the GKV [5] that the ITG turbulent transport in the helical plasma is reduced when the zonal flow generation is enhanced in the inward-shifted configuration [6, 7]. This qualitatively agrees with the Large Helical Device (LHD) [8] experimental results, which show that the anomalous transport in the inward-shifted cases is reduced with a decrease in the radial drift of ripple-trapped particles [9], even with an increase in the unfavorable field line curvature [10].

To understand the transport physics of confinement plasmas better, quantitative comparisons between the experimental observations and the computational simulations with the experimental conditions should be done. In the GKV simulations, the model helical field given by the limited number of Fourier components are employed with the large-aspect-ratio approximation for the flux surface geometry. Under the approximation, the simplified Jacobian and metric are used for each term in the gyrokinetic equation. For more quantitative gyrokinetic simulations, it is a natural path to furnish a well-established gyrokinetic code with detailed geometrical information obtained from three-dimensional equilibrium calculations as in Refs. [11–13]. We develop a new gyrokinetic Vlasov flux-tube code, GKV-X [14], which precisely deals with realistic magnetic configurations in non-axisymmetric systems. The GKV-X uses the geometrical information provided from the VMEC code, which is a standard three-dimensional magnetohydrodynamic equilibrium solver. Using the GKV-X, we investigate the effects of the geometry and the collision of the LHD plasmas on the ITG modes, the geodesic acoustic modes (GAM), and the zonal flow responses by the benchmark tests against the GKV calculation, and also the comparisons between the GKV-X linear simulations and the LHD experimental observations for the ITG modes and zonal flows.

The rest of this paper is organized as follows. In Sec. 2, we briefly describe the GKV-X and the basic equations employed in the calculation. In Sec. 3, simulation results obtained by the GKV-X are shown, and the geometrical and collisional effects on the ITG modes and zonal flows are discussed. In Sec. 4, comparisons between the linear simulations and the experimental measurements in the LHD high ion temperature discharges are performed. Section 5 presents the summary of the study.

2. GKV-X Code

The GKV-X is a gyrokinetic Vlasov flux-tube code which incorporates full geometrical information of the non-axisymmetric confinement field, as well as Fourier components of the field obtained from VMEC calculation. The magnetic field strength is represented as

$$B = \sum_{n=0}^{n_{\max}} B_{0n}(\rho)\cos n\zeta + \sum_{m=1}^{m_{\max}} \sum_{n=-n_{\max}}^{n_{\max}} B_{mn}(\rho)\cos(m\theta - n\zeta), \tag{1}$$

in the Boozer coordinate system $\{\rho,\theta,\zeta\}$, where the flux labeling index $\rho \equiv \sqrt{\Psi/\Psi_a}$ is defined by the toroidal magnetic flux $\Psi = B_{\rm ax} r^2/2$ at the minor radius r, and Ψ_a at the last closed surface $r = a$. $B_{\rm ax}$ is the field strength at the magnetic axis, $B_{mn}(\rho)$ is the Fourier component with the poloidal and toroidal mode numbers (m,n), and the maximum mode numbers in the VMEC calculation $m_{\max}$ and $n_{\max}$. From the flux surfaces obtained from the equilibrium in the cylindrical coordinates $\{R,Z,\phi\}$, the metric tensors g_{ij}, g^{ij}, and the Jacobian $\sqrt{g}$ on the flux surface can also be obtained as

$$g_{ij} = \frac{\partial R}{\partial i}\frac{\partial R}{\partial j} + \frac{\partial Z}{\partial i}\frac{\partial Z}{\partial j} + R^2\frac{\partial \phi}{\partial i}\frac{\partial \phi}{\partial j}, \quad g^{il} = \frac{1}{g}\left(g_{jm}g_{kn} - g_{jn}g_{km}\right), \tag{2}$$

$$\sqrt{g} = (\nabla\rho\times\nabla\theta\cdot\nabla\zeta)^{-1} = \frac{\Psi'}{B^2}\left(B_\zeta + q^{-1}(\rho)B_\theta\right), \tag{3}$$

where q is the safety factor, and the prime symbol represents the derivative with respect to ρ. The code uses the local flux-tube model [16] with the field-aligned coordinates $\{x,y,z\} = \{r - r_0, (r_0/q_0)\left[q(\rho)\theta - \zeta\right], \theta\}$ with the safety factor q_0 at the minor radius $r_0 = \rho_0 a$. The coordinate $z = \theta$ is regarded as a coordinate along the field line labeled by $\alpha = \zeta - q(\rho)\theta = $ const. The GKV-X solves the gyrokinetic equation for the perturbed ion gyrocenter distribution function δf, in the low-β electrostatic limit,

$$\left(\frac{\partial}{\partial t} + v_{||}\boldsymbol{b}\cdot\nabla + \frac{c}{B}\boldsymbol{b}\times\nabla\Phi\cdot\nabla - \frac{\mu}{m_{\rm i}}\boldsymbol{b}\cdot\nabla B\frac{\partial}{\partial v_{||}} + \boldsymbol{v}_{\rm d}\cdot\nabla\right)\delta f = \left(\boldsymbol{v}_* - \boldsymbol{v}_{\rm d} - v_{||}\boldsymbol{b}\right)\cdot\frac{e\nabla\Phi}{T_{\rm i}}F_{\rm M} + C(\delta f), \tag{4}$$

where $F_{\rm M}$ is the Maxwellian distribution, $C(\delta f)$ is the collision term, $v_{||}$ and μ represent the parallel velocity and the magnetic moment, respectively. In the GKV-X, we employ each term in Eq.(4) with exact forms. The magnetic and diamagnetic drift velocities are denoted by $\boldsymbol{v}_{\rm d}$ and $\boldsymbol{v}_*$, respectively. The electron density is assumed to be adiabatic, and the electrostatic potential Φ is calculated from the quasi-neutrality condition. The magnetic drift frequency $\omega_{\rm d} = \boldsymbol{k}_\perp\cdot\boldsymbol{v}_{\rm d}$, and the diamagnetic drift frequency $\omega_* = \boldsymbol{k}_\perp\cdot\boldsymbol{v}_*$ with zero-beta are given by

$$\omega_{\rm d} = -\frac{c}{eB^2}\frac{a}{\sqrt{g}}\left(\mu + \frac{1}{B}m_{\rm i}v_{||}^2\right)\left[k_y\left[\left(\frac{\rho_0}{q_0}B_\rho + \hat{s}\theta B_\zeta\right)\frac{\partial B}{\partial\theta}\right.\right.$$

$$+\left(\rho_0 B_\rho - \hat{s}\theta B_\theta\right)\frac{\partial B}{\partial \zeta} - \left(\frac{\rho_0}{q_0}B_\theta + \rho_0 B_\zeta\right)\frac{\partial B}{\partial \rho}\Bigg] + k_x\left[B_\zeta\frac{\partial B}{\partial \theta} - B_\theta\frac{\partial B}{\partial \zeta}\right]\Bigg], \quad (5)$$

$$\omega_* = -\frac{cT_\mathrm{i}}{e}\frac{\rho_0 a^2}{\Psi'}k_y\left[\frac{1}{L_n} + \frac{1}{L_T}\left(\frac{m_\mathrm{i}v^2}{2T_\mathrm{i}} - \frac{3}{2}\right)\right], \quad (6)$$

with the perpendicular wavenumbers (k_x, k_y), the magnetic shear parameter $\hat{s} = (\rho_0/q_0)q'$, and the background gradient scale length for the density and temperature defined by $L_n^{-1} = -\mathrm{d}\ln n/\mathrm{d}r$, and $L_T^{-1} = -\mathrm{d}\ln T_\mathrm{i}/\mathrm{d}r$, respectively. Using the metric tensors and the Jacobian, the perpendicular wavenumber and the parallel derivative can be calculated as

$$k_\perp^2 = k_x^2 a^2 g^{\rho\rho} + 2k_x k_y a^2\left[\hat{s}\theta g^{\rho\rho} + \frac{\rho_0}{q_0}\left(q_0 g^{\rho\theta} - g^{\rho\zeta}\right)\right]$$
$$+k_y^2 a^2\left[\frac{\rho_0^2}{q_0^2}\left(g^{\zeta\zeta} + q_0^2 g^{\theta\theta} - 2q_0 g^{\theta\zeta}\right) + 2\hat{s}\theta\frac{\rho_0}{q_0}\left(q_0 g^{\rho\theta} - g^{\rho\zeta}\right) + \hat{s}^2\theta^2 g^{\rho\rho}\right], \quad (7)$$

$$\boldsymbol{b}\cdot\nabla = \frac{\Psi'}{q_0 B\sqrt{g}}\left(\frac{\partial}{\partial\theta} + q_0\frac{\partial}{\partial\zeta}\right). \quad (8)$$

3. Geometrical and Collisional Effects on ITG modes and Zonal-flows

In order to investigate the effects of non-axisymmetric geometry on the ITG modes and zonal flows, gyrokinetic Vlasov simulations using linearized versions of the GKV-X and GKV are performed in the helical systems. We prepare the field configuration with the parameters of the confinement field based on the VMEC results for the standard LHD case, which is close to the "S-B case" in Ref. [17]. In the GKV-X simulation, we use the VMEC configuration with a lot of helical components. The GKV calculation uses the parameters which are obtained from the VMEC configuration in terms of the toroidal, main helical, two side-band components, and their radial derivatives. In both the calculations, we use the same parameters for the variables, $L_n/L_T = 3$, $T_\mathrm{e}/T_\mathrm{i} = 1$, $L_n/R_0 = 0.3$, $q_0 = 1.9$, $\hat{s} = -0.87501$, and $\alpha = 0$.

3.1. Geometrical Effects

The growth rates and real frequencies of the ITG modes are shown in Fig.1 as functions of $k_y\rho_\mathrm{i}$ which are obtained from the both codes. Here, ρ_i is the ion gyroradius. The plots are evaluated at $\rho = 0.6$ and $k_x = 0$. Compared to the GKV calculation, the growth rate obtained from the GKV-X is slightly higher for $k_y\rho_\mathrm{i} \lesssim 0.3$ and lower for $k_y\rho_\mathrm{i} \gtrsim 0.3$, and the real frequency in the GKV-X simulation is slightly more negative than that in the GKV. The differences between the two codes are enhanced with the increasing poloidal wavenumber, which originates from the ripple components and full metric tensor through ω_d and $k_\perp$, respectively. Because ω_d in the GKV-X includes more helical ripple components than in the GKV, the difference of ω_d appears clearly, and that in the GKV-X is more negative than in the GKV around $z \simeq 0$, where the ITG modes are destabilized by unfavorable magnetic field line curvature. According to Eq.(5), the difference in ω_Di is enhanced in the large $|k_y|$ region. In Eq.(7), the terms including the metric tensor components $g^{\theta\theta}$ and $g^{\rho\rho}$, which reflect the shape of the elliptic magnetic surface, are influential in $k_\perp$ related to the finite gyroradius effect. The term with $g^{\theta\theta}$ remains finite around $z \simeq 0$, and the contribution of the term to $k_\perp$ is also enhanced for higher poloidal wavenumbers, while the term with $g^{\rho\rho}$ vanishes at $z = 0$. In the the diamagnetic drift frequency and the mirror force term, the differences between the two codes are much smaller than those in ω_d and $k_\perp$. At large poloidal wavenumbers, therefore, the helical ripple components of the confinement field

and the metric tensor of the magnetic surface affect the frequency and the growth rate of the ITG modes through the magnetic drift frequency and the finite gyroradius effect.

Eigenfunctions of the electrostatic potential ϕ_k are also compared for $k_y\rho_i = 0.324$ and $k_y\rho_i = 0.649$ in Fig.2. As seen in the figure for $k_y\rho_i = 0.324$, the mode structures of ϕ_k obtained by the two codes have almost same profiles, which is accompanied by oscillations associated with the helical ripples. On the other hand, the profiles for larger poloidal wavenumber ($k_y\rho_i = 0.649$) show different ripple structures in the unfavorable curvature region around $z \simeq 0$. This is consistent with the results of the growth rate and the real frequency shown in Fig.1, where the differences are found mainly in the higher poloidal wavenumbers.

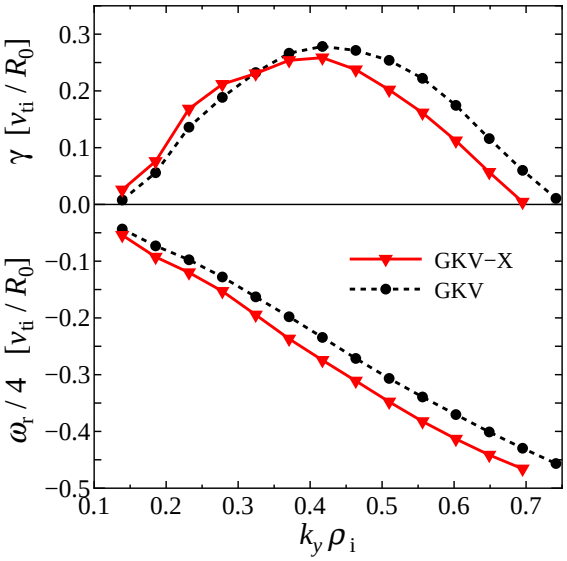

FIG. 1: Growth rates (top) and real frequencies (bottom) of the ITG mode obtained from the GKV *(black circles) and the* GKV-X *(red triangles).*

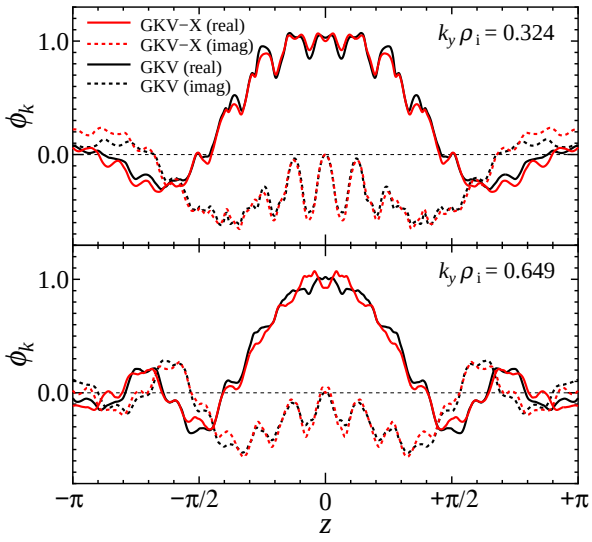

FIG. 2: Eigenfunctions of electrostatic potential ϕ_k for $k_y\rho_i = 0.324$ (top) and $k_y\rho_i = 0.649$ (bottom) at $k_x = 0$, with the real and imaginary parts.

Figure 3 shows the response functions of the flux surface averaged zonal flow potentials to the initial perturbation, $\langle\phi_{k_\perp}(t)\rangle/\langle\phi_{k_\perp}(0)\rangle$ during their linear collisionless damping obtained from the GKV-X and GKV simulations for two different radial wavenumbers, $k_x\rho_i = 0.0637$ and $k_x\rho_i = 0.1274$. As seen in the plots, the response functions given by the two codes agree well with each other for both k_x values. The residual levels of the zonal flow potentials at $t/(R_0/v_{ti}) \sim 30$ are obtained as $\mathcal{K}_{\text{GKV-X}} = (1.33 \pm 0.81) \times 10^{-2}$, $\mathcal{K}_{\text{GKV}} = (1.32 \pm 0.79) \times 10^{-2}$ for $k_x\rho_i = 0.0637$, and $\mathcal{K}_{\text{GKV-X}} = (3.54 \pm 0.15) \times 10^{-2}$, $\mathcal{K}_{\text{GKV}} = (3.36 \pm 0.10) \times 10^{-2}$ for $k_x\rho_i = 0.1274$. Thus, the effect of the geometry on the residual zonal flow levels is very weak. It is considered that the ripple effect of the perpendicular

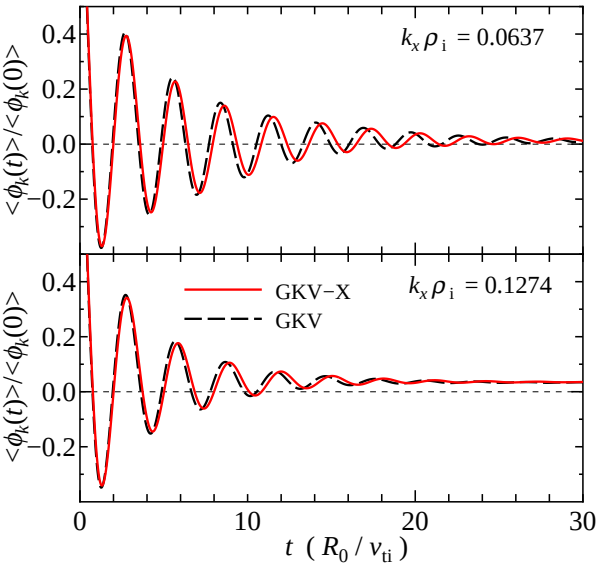

FIG. 3: Linear responses of the zonal flow potentials for the GKV *simulation with model field (black dashed curves) and* GKV-X *simulation with VMEC field configuration (red solid curves).*

Table 1: *Peak positions of the density fluctuations observed in the LHD experiment and the ITG growth rates obtained in the* GKV-X *simulations.*

	Low-T_i		High-T_i	
	ρ_{peak}	$(k\rho_i)_{peak}$	ρ_{peak}	$(k\rho_i)_{peak}$
Experiment	0.8 - 1.0	0.26	0.6 - 0.8	0.45
Simulation	0.83	0.20	0.65	0.35

wavenumber given in Eq.(7) for the GKV-X case is eliminated by taking the flux surface average in calculation of the zonal flow potential that loses the poloidal-angle-dependent components associated with GAM oscillations.

3.2. Collisional Effects

For the case of the LHD field at $\rho \simeq 0.6$, the time evolution of the zonal flow potentials is investigated by the GKV-X with the finite collisions including the pitch angle scattering in which the collision time of $\tau_{ii} \simeq 150(R_0/v_{ti})$ corresponding to the ion density $n_i \simeq 1.0 \times 10^{19}\mathrm{m}^{-3}$ and the temperature $T_i \simeq 2.0$ keV. This weak collisionality does not influence the growth rate and the real frequency of the ITG modes in Fig.1, because $\gamma, \omega_r \gg \tau_{ii}^{-1}$ in this case. However, we see from the response functions in Fig.4 that, by the small collisionality, the residual zonal flow level is reduced to a half of the collisionless case at $t \sim 30(R_0/v_{ti}) \sim 0.2\tau_{ii}$, even if the GAM oscillation is not affected. Therefore, the weak collisionality is considered to enhance the turbulent transport by reducing the zonal flows as claimed in Ref. [18].

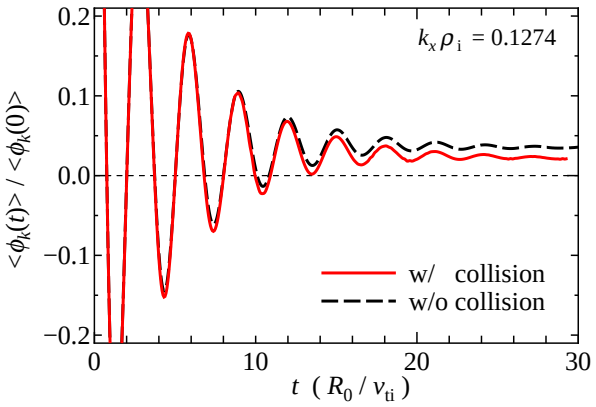

FIG. 4: Linear responses of the zonal flow potential obtained by the GKV-X *with collision (red solid curves) and without collision (black dashed curves). Both figures are obtained at* $\rho \simeq 0.6$.

4. Comparison with LHD Experiment

In recent Large Helical Device (LHD) experiments, high ion temperature discharges have been realized by the high power neutral beam injection, and spatial profiles of density fluctuations in radial, wavenumber, and phase velocity spaces are measured by phase contrast imaging (PCI) [19]. The observed fluctuations most likely propagate in the direction of ion diamagnetic rotation in the plasma frame, and their amplitudes increase with growth of the temperature gradient [20]. The results show the typical characteristics of the ITG turbulence. In Table.1, the positions in k-ρ space where the observed fluctuation increases are shown for the different temperature profiles, low-T_i phase ($t = 1.833$ s) and high-T_i phase ($t = 2.233$ s). In the low-T_i phase, the phase velocity of the fluctuation for $\rho \gtrsim 0.9$ is also evaluated in the plasma frame as $v^{exp} \sim -2.5 \times 10^3$ [m/s], although that for the high-T_i phase at $\rho \sim \rho_{peak}^{sim}$ cannot be obtained since the measurements of $v_{E\times B}$ are limited to $\rho \gtrsim 0.8$ in the high-T_i phase. Here, the minus sign represents the direction of the ion diamagnetic rotation.

In order to investigate the characteristics of the density fluctuations observed in the experiment, the linear gyrokinetic simulations are performed by using GKV-X in the equilibrium magnetic field configuration corresponding to the discharge obtained from the VMEC calculation with the experimental profiles of the temperature and the density. The comparisons between the simulation results and the experimental observations are also done.

4.1. ITG Growth Rates Profiles

Figures 5 shows the simulation results of the growth rates and real frequencies of the ITG modes as functions of $k_y\rho_i$ in the low-T_i and high-T_i phases. In the plots, the maximum values of γ can be obtained for each radial position. For example, at $\rho = 0.65$ in the high-T_i phase, the maximum growth rate is $\gamma_{max} \sim 0.25\ (v_{ti}/R_0)$ with $k_y\rho_i \sim 0.35$. Thus, we obtain the radial profiles of γ_{max} rates as shown in Fig.6. From the plots, we can find the peaks of γ_{max} as shown in Table.1. Comparing the results with the fluctuation measurements in the LHD discharge, the peak regions of the density fluctuations are located around the positions where the ITG modes are most unstable in radial and wavenumber spaces. From the value of the real frequencies, the phase velocities at $\rho = \rho^{sim}_{peak}$ in the plasma frame, $v^{sim} = \omega_r^{sim}/k_y$, can also be roughly estimated as $v^{sim} \sim -2.0 \times 10^3$ [m/s] (low-T_i phase), and $v^{sim} \sim -1.0 \times 10^4$ [m/s] (high-T_i phase). In the low-T_i phase, the phase velocity quantitatively agrees with the experimental value v^{exp} for $\rho \gtrsim 0.9$ as presented in the top of this section. From the results, therefore, the fluctuation peaks observed in the LHD experiments are considered to be mainly driven by the ITG modes.

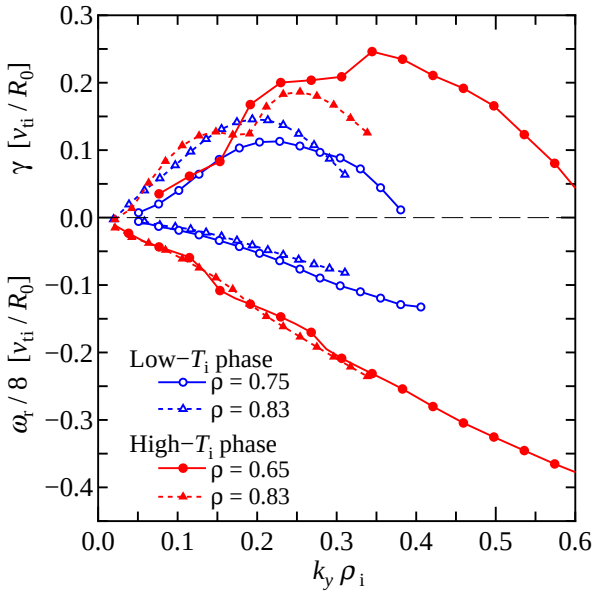

FIG. 5: Growth rates (top) and real frequencies (bottom) of the ITG modes for the low-T_i phase (blue symbols) and high-T_i phase (red symbols).

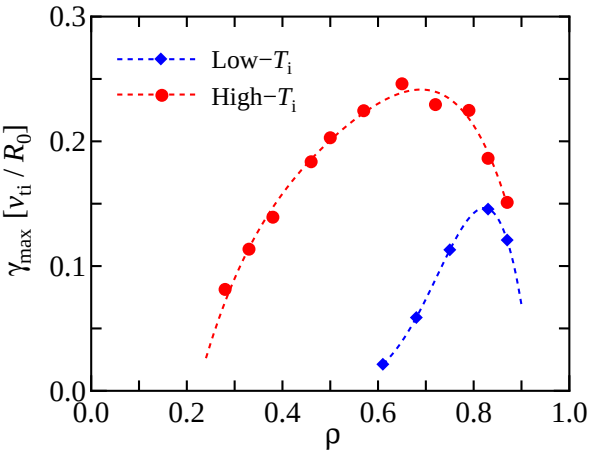

FIG. 6: Radial profiles of γ_{max} for the low-T_i phase (blue diamonds) and the high-T_i phase (red circles).

4.2. Critical Ion Temperature Gradients

The critical ion temperature gradients for the ITG mode are also evaluated by investigating the dependence of the ITG growth rates on the temperature gradient. In Fig.7, the critical values for the low- and high-T_i phases are shown as functions of ρ. Paying attention to the deviation of the temperature gradient from the critical value in the figure, we find that γ_{max} given by Fig.6 peaks at a radial position where the deviation is largest. The critical values are higher than

the experimental values for $\rho \lesssim 0.6$ in low-T_i phase, and $\rho \lesssim 0.2$ in high-T_i phase, where γ_{max} of Fig.6 vanishes. Comparing the radial profiles of the critical temperature gradient between the two phases, the critical values for the high-T_i phase are higher than those for the low-T_i-phase. Therefore, it is considered that the higher critical temperature gradient may contribute to the improvement of the confinement capability. In fact, the magnetic drift frequency ω_d for the high-T_i phase is slightly shifted into the positive direction around $z \sim 0$, which implies more favorable magnetic curvature for stabilization of the ITG mode than for the low-T_i phase. In addition, lower density gradients for the high-T_i phase are considered to also contribute to higher critical temperature gradients than for the low-T_i phase.

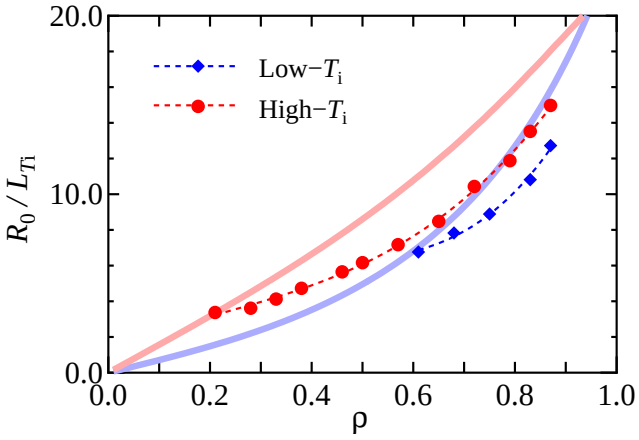

FIG. 7: Radial profiles of the critical temperature gradient in the low-T_i phase (blue diamonds) and high-T_i phase (red circles). Bold curves with light blue and light red colors represent the experimental profiles of R_0/L_{Ti} in the low- and high-T_i phases, respectively.

5. Summary

In this work, the GKV-X code is developed, which is applicable to non-axisymmetric configuration such as the LHD, including the collision effects, full information about the metric tensor, Jacobian, and Fourier components of the helical field obtained from the VMEC equilibrium calculation. Making use of the GKV-X, we investigate the effects of the geometry of the confinement field and the collisions on the ITG modes and the zonal flows in the helical systems. It is found from the simulations that the effects of full geometry and helical ripples are prominent for higher poloidal wavenumbers due to the finite gyroradius effect and the magnetic drift frequency. The dampings of the zonal flow potential are also examined, and the weak collisionality is considered to enhance the turbulent transport with reduction of the zonal flows.

The comparisons of the GKV-X calculations with the density fluctuation measurements in the LHD high-T_i discharges are also performed. In the simulation results of the focused discharge, the unstable ITG modes have the growth rates which peak at radial positions with the largest deviation of the temperature gradient from the critical values. The peak positions of the growth rate are close to the regions where the density fluctuation peaks are measured in the experiment. The critical temperature gradients in the high-T_i phase are higher than those in the low-T_i phase. More favorable magnetic curvature and lower density gradient realized in the high-T_i phase are considered to contribute to this up-shift of the critical T_i gradient and accordingly the achievement of the high T_i gradient. Also, the phase velocities of the ITG modes obtained from the simulation agree with the experimental observations. From the results, therefore, it is considered that the increases of the fluctuations measured in the experiment are mainly attributed to

the ITG instability. The nonlinear simulation of the ITG turbulence for the LHD experimental conditions is currently in progress as the next step of this work.

Acknowledgments

One of the authors (M.N.) would like to thank to Dr. S. Satake for useful information about the LHD equilibrium and the VMEC code, and also Prof. K.Y. Watanabe about equilibrium calculation in the LHD experiments. This work is supported in part by the Japanese Ministry of Education, Culture, Sports, Science and Technology, Grant No. 22760660, and 21560861, and in part by National Institute for Fusion Science Collaborative Research Program, NIFS09KTAL022, NIFS08KDAD008, NIFS08KTAL006, NIFS08KNXN14, NIFS10KDAT020, and NIFS10KNXN186. Numerical calculations are carried out by use of the Plasma Simulator and the LHD numerical analysis system at National Institute for Fusion Science.

Reference

[1] HORTON, W., Rev. Mod. Phys. **71**, 735 (1999).
[2] DIAMOND, P.H., ITOH, S.-I., ITOH, K. and HAHM, T.S., Plasma Phys. Control. Fusion **47**, R35 (2005).
[3] ITOH, K., ITOH, S.-I., DIAMOND, P.H. and FUJISAWA, A., Phys. Plasmas **13**, 055502 (2006).
[4] FUJISAWA, A., Nucl. Fusion **49**, 013001 (2009).
[5] WATANABE, T.-H. and SUGAMA, H., Nucl. Fusion **46**, 24 (2006).
[6] WATANABE, T.-H., SUGAMA, H. and FERRANDO-MARGALET, S., Phys. Rev. Lett. **100**, 195002 (2008).
[7] SUGAMA, H., WATANABE, T.-H. and FERRANDO-MARGALET, S., Plasma Fusion Res. **3**, 041 (2008).
[8] MOTOJIMA, O., OHYABU, N., KOMORI, A. et al., Nucl. Fusion **43**, 1674 (2003).
[9] YAMADA, H., KOMORI, A., OHYABU, N. et al., Plasma Phys. Controlled Fusion **43**, A55 (2001).
[10] KURODA, T. and SUGAMA, H., J. Phys. Soc. Jpn. **70**, 2235 (2001).
[11] XANTHOPOULOS, P. and JENKO, F., Phys. Plasmas **13**, 092301 (2006).
[12] XANTHOPOULOS, P., COOPER, W.A., JENKO, F. *et al.*, Phys. Plasmas **16**, 082303 (2009).
[13] MYNICK, H.E., XANTHOPOULOS, P. and BOOZER, A.H., Phys. Plasmas **16**, 110702 (2009).
[14] NUNAMI, M., WATANABE, T.-H. and SUGAMA, H., Plasma Fusion Res. **5**, 016 (2010).
[15] HIRSHMAN, S.P. and BETANCOURT,O., J. Comput. Phys. **96**, 99 (1991).
[16] BEER, M.A., COWLEY, S.C. and HAMMETT, G.W., Phys. Plasmas **2**, 2687 (1995).
[17] FERRANDO-MARGALET, S., SUGAMA, H. and WATANABE, T.-H., Phys. Plasmas **14**, 122505 (2007).
[18] LIN, Z., HAHM, T.S., LEE, W.W. *et al.*, Phys. Plasmas **7**, 1857 (2000).
[19] TANAKA, K. MICHAEL, C.A., VYACHESLAVOV, L.N. *et al.*, Rev. Sci. Instrum. **79**, 10E702 (2008).
[20] TANAKA, K. MICHAEL, C.A., VYACHESLAVOV, L.N. *et al.*, to appear in Plasma Fusion Res.
[21] IDA, K., YOSHINUMA, M., OSAKABE, M. *et al.*, Phys. Plasmas **16**, 056111 (2009).